3D direct pore level simulations of radiant porous burners

Christoph Wieland [a],*, Christof Weis [b], Peter Habisreuther [c], Dimosthenis Trimis [b]

[a] *DVGW Research Center at the Engler-Bunte Institute of the Karlsruhe Institute of Technology, Engler-Bunte-Ring 1-9, 76131 Karlsruhe, Germany*
[b] *Engler-Bunte-Institute Combustion Technology, Karlsruhe Instutute of Technology, Engler-Bunte-Ring 7, 76131 Karlsruhe, Germany*
[c] *Institute for Technical Chemistry, Karlsruhe Institute of Technology, Hermann-von-Helmholtz-Platz 1, 76344 Eggenstein-Leopoldshafen, Germany*

A B S T R A C T

Inside porous burners, chemical combustion reactions coincide with complex interaction between thermo-physical transport processes that occur within solid and gaseous phase and across phase boundary. Fluid flow, heat release and resulting heat flows influence each other. The numerical model used in this work considers gaseous and solid phases, includes fluid flow, enthalpy transport, conjugate heat transfer, and radiative heat transfer between solid surfaces, as well as combustion kinetics according to a skeletal chemical reaction mechanism, fully resolved on the pore scale in three-dimensional space (Direct Pore Level Simulation, DPLS). The calculations are performed based on the finite volume method using standard applications implemented in the OpenFOAM library. The present study presents simulations of three different structures, each at four settings of specific thermal power. Results indicate that specific surface area of the porous structure is a major influencing parameter for increasing radiation efficiency, whereas no correlation of the orientation of an anisotropic structure on radiation efficiency was observed.

1. Introduction

The term *ceramic* covers a range of nonmetallic, inorganic materials, mostly oxide, carbide, nitride or boride metal compounds or mixtures of such. In modern processes, advanced ceramics are applied to exploit special properties such as hardness, chemical inertness, thermal stability, or combinations of those [1]. In ceramic porous media, the ceramic material forms a rigid matrix whose cavities (pores) are filled with a fluid. Open pore configurations are characterized by interconnected cavities, permitting fluid flow through the solid ceramic matrix. Such ceramic porous media are used in various industrial applications such as catalyst support [2], liquid metal filtration [3], heat exchangers [4], high temperature thermal energy storage [5], volumetric receivers [6] or radiant porous burners [7].

Traditional manufacturing processes of ceramic porous media produce foam-like structures [8] that are associated with certain ranges in size and form of the void cells and solid elements. An advanced technology that builds upon additive manufacturing of polymeric precursors and successive ceramic replication offers the opportunity to manufacture geometrically defined ceramic struc-

tures [9]. This technology offers a wide range of design opportunities and has been applied to volumetric receivers in laboratory scale experiments [10]. In such receivers, the solid porous medium is heated by absorption of concentrated solar radiation. Subsequently, the heat is transferred to a fluid that flows through the porous medium.

A similar application for ceramic porous media with inverse heat fluxes is the volumetric porous burner, where heat is provided from the fluid phase and thermal radiation is emitted by the solid structure. Radiant porous burners following a two layer design [11] consist of a flame trap and an open pore solid in which heat release due to combustion occurs. The flame trap is a perforated plate made of mullite fiber, a ceramic material with low thermal conductivity. The unburned premixed air-fuel mixture passes the flame trap through a pattern of straight circular ducts. The porous structure is made of silicon-infiltrated silicon carbide (Si-SiC), a ceramic composite material resistant to thermal and mechanical stresses in an oxidative high temperature environment [12]. Heat release associated with the combustion reaction within the cavities of the Si-SiC heats the porous structure up to a temperature in the order of the gas temperature. At this high temperature, the solid material emits intensive thermal radiation. The flame trap prevents from upstream flame propagation by the combined effect of inducing a gas velocity exceeding the flame speed and thermal quenching by comparatively small dimensions in the

* Corresponding author.
  E-mail address: christoph.wieland@partner.kit.edu (C. Wieland).

ducts. With its low thermal conductivity, the flame trap also has the effect of a thermal barrier between the downstream high temperature combustion zone and an upstream mixing and gas distribution zone. Such porous burners feature high emission of thermal radiation and low emission of hazardous nitrogen oxides [13]

Performance of a porous burner results from chemical and thermophysical processes and conditions inside the burner that are interdependent and interrelated with the solid structure. Advanced control over the solid structure's geometry offers the opportunity of process optimization; however, detailed knowledge of the complexly connected mechanisms of heat release and heat transfer are required for such an optimization.

Most literature on porous burners refers to non-ordered solid structures in the form of packed beds or foams. Experimental investigations cover flame stability limits [14–16], effective flame speed [17], pollutant emissions [15,18,19], and thermal radiation [18,20,21]. Temperature profiles inside the porous medium were obtained by intrusive [16–18,22–24] and non-intrusive [25] methods. Flame front detection was performed by laser-optical species detection [26], by x-ray tomography [27] and lately with a high speed photo camera and a thin model porous burner [28].

Numerical investigations cover the range from detailed three dimensional to simplified one dimensional considerations. One dimensional models use effective parameters to reproduce the impact of the solid phase on the combustion process e.g. by means of a volumetric heat transfer coefficient, axial dispersion of species or heat, effective conductivity or extinction coefficient [29–34]. Correlation factors for the effective parameters were derived from correlations for packed beds [35], from dedicated experiments [36], or from numerical simulations with μ-CT scans [37–39]. With comparable low computational effort for a single simulation, one dimensional models are suitable for parametric surveys such as [40], where the impact of different effective parameters on porous burners has been studied.

In two dimensional models, radial gradients and distribution of temperature and species are captured in homogeneous [41] and heterogeneous [24,42,43] consideration of gaseous and fluid phase. The importance of local thermal non-equilibrium has been demonstrated for volume averaged models [44] as well as for geometrically resolved models [43]. For a porous micro-combustor with systematically arranged porous structure, a pore-scale model resulted in more accurate predictions than the volume averaged model [45]. For the simplified case of combustion in a narrow channel, Miyanta et al. showed an increased thermal flame thickness well above 1 mm by direct numerical simulation [46]. Ferguson et al. rated a mesh resolution of 100 μm as sufficient for capturing flame stabilization in two dimensional simulation of porous media combustion [42].

Three-dimensional numerical simulations of porous burners with processes resolved on pore scale require significant computational effort and are rarely found in the literature. Bedoya et al. simulated combustion of methane (CH_4) in a divergent random foam based porous medium in 3D DPLS employing a single step reaction mechanism and neglecting radiation [17]. They deduced a probability density function of local temperature for application in one-dimensional models of porous media combustion. Hoda et al. investigated a two layer porous burner with gaseous and solid phases homogenized in local thermal non-equilibrium, accounting for radiation with a discrete ordinate method [47]. They altered macroscopic radiative properties of the porous medium and found that an increased optical thickness and reduced scattering albedo have beneficial impact on radiation output. Yakovlev et al. performed 3D DPLS of CH_4 combustion in a packed bed and investigated flame stabilization in thin layered porous burners, employing a detailed chemical mechanism and considering radiation in a view-factor model [48,49]. They found that the structure of
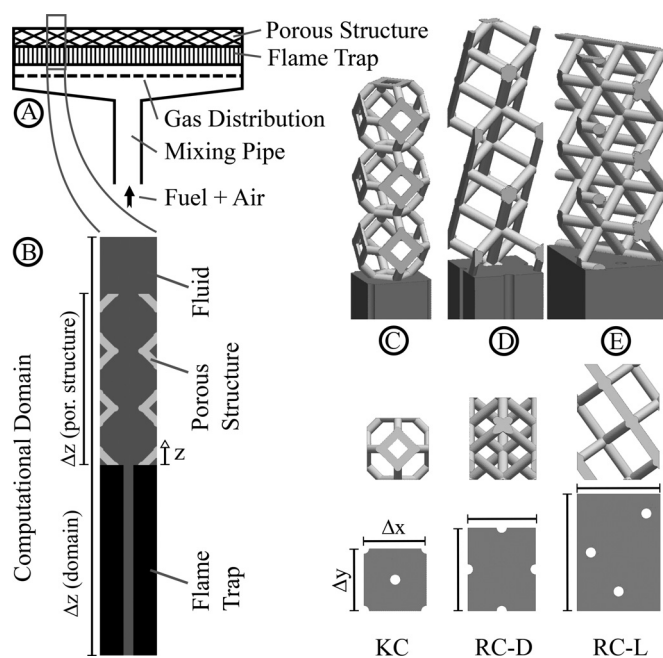
Fig. 1. A) Schematic drawing of flat two layer porous radiant burner; B) Sketch of the computational domain cross section; C)-E) Solid domain parts left to right: KC, RC-D, RC-L; top to bottom: 3D-view on structures, top view on porous structures, flame trap hole pattern.

the porous matrix has significant impact on the interrelated processes and expect underestimation of heat transfer for volume-averaged models. For thin layered radial porous burners they identified three regimes of flame stabilization. Billerot et al. simulated a representative element of a single layer porous burner in pore level resolution with a single step reaction mechanism and accounting for radiation with a discrete ordinate method [50]. Their porous structure refers to a geometry produced with additive manufacturing technology. For their structure of 46% porosity they find negligible contribution of radiative heat transfer compared to conduction.

Continuous research on porous burners in recent decades has promoted insight into porous media burners and covered a wide range of applications [51]. However, for the efficient application of new manufacturing opportunities, understanding of the solid's structural parameters impact on phenomena like flame position and heat transfer need to be improved.

The present study is focused on the net radiative emission of two layer porous burners and on the impact of different well defined porous structures. 3D DPLS of radiant porous burners, employing a skeletal chemical reaction mechanism and a finite volume discrete ordinate method (fvDOM) are used to examine three different porous structure setups at different loads of thermal power. Integral radiation efficiency is determined, load dependency of internal fields and structure dependency of heat transfer at the gas-solid interface are investigated.

2. Numerical methods

2.1. Numerical domain

The investigated design of a typical planar radiant porous burner is shown in Fig. 1 A; it comprises a pipe for pre-mixing air and fuel, the gas distribution device, the flame trap, and the porous structure. Numerical simulation of the entire device with the 3D DPLS approach including radiative heat transfer is an unreasonable task from computational effort point of view. For the

Table 1
Geometric information on the three setups.

	Number of Cells	Domain Dimensions			Porous Structure	Porosity	Specific Surface Area
		Δx	Δy	Δz	Δz	ϵ	S_V
Units	10^6	mm	mm	mm	mm	-	m^{-1}
KC	6.8	6.0	6.0	44.0	18.0	90.0%	471
RC-D	5.1	6.5	8.0	46.5	22.5	90.3%	362
RC-L	7.8	8.0	11.3	43.5	19.5	90.4%	365

present study, we therefore neglect the mixing pipe and gas distribution section and assume the gas as homogeneously mixed and distributed at the inlet of the flame trap. Lateral extents of the burner plate are reduced to a representative element of the considered porous structure. In the present work, the porous structures are composed of periodic repeatable structure elements termed as 'unit cells'. By application of periodic boundary conditions to the unit cell in lateral directions comparable to [50], the simulated structure is treated as a representative element of an infinitely expanded planar radiant porous burner. This approach excludes radial losses and focuses on the impact of structures and their orientation on axial radiation emission. Constriction of the computational domain in lateral dimensions introduces limitation in the possible lateral extents of flow field patterns. With the maximal lateral extensions of the cavities captured and high surface-to-volume ratio in the present setups of regular porous structures, confident assumption is made that the application of representative unit cells is valid.

The resulting simulation domain (Fig. 1B) covers the unit cell's extents in lateral directions; in axial direction it comprises the entire dimension of flame trap and porous structure, and an additional space between the porous structure and the outlet boundary. In the present work, we focus on unit cell based structures that are composed as three-dimensional networks of solid cylindrical struts. These geometric models are comparable to the real defined porous structures for burners produced with the replica technique [9]; however, the technical structures have hollow struts that originate form the polymeric precursors [52]. Two different unit cells, namely the Kelvin Cell (KC) and the Rotated Cube (RC) are investigated. The Kelvin cell, also known as tetrakaidecahedron, is a widely spread model for open-cell foams [53,54]. A KC unit cell of 6 mm size in axial and lateral directions was used; the stack of three unit cells in axial direction corresponds to a structure height of 18 mm (Fig. 1 C). The Rotated Cube structure is based on the edges of a cube and has been applied e.g. in heterogeneous catalysis applications as a catalyst support [55]. The RC unit cell in this work has extents of 6.3 mm × 8.0 mm × 11.3 mm and is applied in two different orientations, a 'dense' (RC-D) configuration with high optical blockage in axial direction and a 'light' (RC-L) configuration with low optical blockage in axial direction. Two RC unit cells are stacked for the RC-D structure (Fig. 1D) and three unit cells for the RC-L structure (Fig. 1E), corresponding to an axial structure dimension of 22.5 mm and 19.5 mm, respectively. The volume spanned by the structure's dimensions is used to determine porosity $\varepsilon = V_{por}/\left(\Delta x \Delta y \Delta z_{por}\right)$ and specific surface area $S_V = A_I/\left(\Delta x \Delta y \Delta z_{por}\right)$ from the porous structure's solid volume V_{por} and the interface area A_I, respectively. All three considered structures have a porosity of 90% and comparable pore volume (118 mm^3 for KC and 97 mm^3 for RC); specific surface area is 471 m^{-1}, 362 m^{-1}, and 365 m^{-1} for KC, RC-D, and RC-L, respectively. RC-D and RC-L are deduced from the same unit cell, therefore the same value for S_V is expected; the deviation is caused by the different values of surface area at the downstream end of the structures. The flame trap geometry features an axial extent of 20 mm and axial ducts of 1 mm in diameter for all three se-

tups. Lateral extents and duct pattern are adjusted in each setup for a uniform pattern with application of periodic boundary conditions. Table 1 summarizes geometrical parameters of the three setups and Fig. 1C–E gives graphical representations of flame trap and porous structure for all three geometry setups.

The computational mesh was created with the snappyHexMesh utility of the OpenFOAM library ([56], version v1912). Resulting meshes are separated into three regions with mesh cell size less than 300 μm for the solid flame trap region and less than 55 μm for the fluid region and the solid porous structure region; the total mesh size ranges from 5 to 8 million cells.

2.2. Numerical model

This section describes the mathematical model, assumptions, governing equations, and boundary conditions that were used to simultaneously simulate the flow and diffusion of the reactive mixture, chemical reactions including heat release, transport of heat in thermally coupled gaseous and solid regions, and radiative heat transfer through the fluid region.

The fluid phase of premixed methane combustion is modeled as perfect gas with the respective equation of state that is formulated for each species K in Eq. (1) [57].

$$\rho_K = \frac{pM_K}{\mathbb{R}T} \quad \text{and} \quad c_{P,K} - c_{V,K} = \frac{\mathbb{R}}{M_K} \tag{1}$$

with density ρ, pressure p, temperature T, molar weight M and ideal gas constant $\mathbb{R}$. c_P and c_V denote the isobaric and isochoric specific heat capacity, respectively.

In line with direct pore simulations in the literature, the fluid flow is assumed as laminar due to low Reynolds numbers [17,49]. Justification of this assumption for the present work is discussed in Section 3. Gravitation, respectively buoyancy effects are neglected in the present case of forced gas convection through the porous medium. The gas is assumed as a Newtonian fluid, viscous heating, gas radiation, and scattering are neglected. The difference in heat capacity of fluid and solid regions results in different time scales for reaching thermal equilibrium. In laboratory experiments, it takes several minutes for the solid phase to reach thermal equilibrium after ignition. In contrast to this, the time scale for chemical reactions is in the order of fractions of a millisecond. In order to compromise between a stable simulation and computational effort, the fluid phase is simulated transiently, while the solid phases are treated in steady state as described at the end of this section.

With these assumptions, equations for balance of mass, momentum, species, and energy in fluid and solid phases denote as Eqs. (2), (3), (4), (5), and (6), respectively. The present study employs the chtMultiRegionFoam solver of the OpenFOAM library ([56], version v2006) for solving this set of governing equations.

$$\frac{\partial \rho}{\partial t} + \nabla \cdot (\rho \vec{u}) = 0 \tag{2}$$

$$\frac{\partial (\rho \vec{u})}{\partial t} + \nabla \cdot (\rho \vec{u}\vec{u}) = -\nabla p + \nabla \cdot \left(\mu \left[\left(\nabla \vec{u} + (\nabla \vec{u})^T \right) - \frac{2}{3} (\nabla \cdot \vec{u}) \hat{I} \right] \right) \tag{3}$$

Table 2
Polynomial coefficients for thermo-physical properties of the solid regions.

		a_0	a_1	a_2	a_3
porous	κ	165.3974	-0.2294	$1.4328 \cdot 10^{-4}$	$-3.0685 \cdot 10^{-8}$
structure	c_p	662.5489	0.5348	-	-
flame	κ	$2.27 \cdot 10^{-2}$	$1.0 \cdot 10^{-4}$	-	-
trap	c_p	312.7912	1.5205	-	-

$$\frac{\partial(\rho Y_K)}{\partial t} + \nabla \cdot (\rho \vec{u} Y_K) = \nabla \cdot \left(\mu_{eff} \nabla Y_K\right) + M_K R_K \tag{4}$$

$$\frac{\partial(\rho h)}{\partial t} + \nabla \cdot (\rho \vec{u} h) - \frac{\partial p}{\partial t} - \nabla \cdot (\alpha \nabla h) = \dot{Q}_{reac} \tag{5}$$

$$0 = \nabla \cdot (\alpha \nabla h) \tag{6}$$

In the above set of equations, $\vec{u}$ denotes the velocity vector, t the time, μ the dynamic viscosity, $\hat{I}$ the unity vector, Y_K the mass-fraction of the K-th species, R_K the species' reaction rate, h the sensible enthalpy, α the thermal diffusivity, and $\dot{Q}_{reac}$ the heat generation due to reaction.

Chemical kinetics are modeled with finite rate chemistry [58].

The skeletal chemical reaction mechanism employed in the present study considers 17 species and 58 chemical reactions [59]. Thermal diffusivity $\alpha = \kappa / (\rho \cdot c_p)$ is defined as function of thermal conductivity κ, density ρ and isobaric heat capacity c_p. For the fluid region, thermodynamic properties ψ of the mixture are approximated as mass-averaged values from the species data ψ_K.

$$\psi_{cell} = \sum_K Y_K \cdot \psi_K \tag{7}$$

Isobaric heat capacity $c_{p,K}$ of the individual specie is calculated from temperature dependent polynomials. The coefficients are also used for calculation of enthalpy H^0 [60].

$$c_p = \mathbb{R}M^{-1}\left(a_5 T^4 + a_4 T^3 + a_3 T^2 + a_2 T + a_1\right) \tag{8}$$

$$H^0 = \mathbb{R}T\left(a_5 T^4/5 + a_4 T^3/4 + a_3 T^2/3 + a_2 T/2 + a_1 + b_1/T\right) \tag{9}$$

Temperature dependent determination of dynamic viscosity μ_K follows the Sutherland model [61] with correlation factors A_S and T_S

$$\mu = \frac{A_S \sqrt{T}}{1 + T_S/T} \tag{10}$$

Thermal conductivity of the gas is modeled according to Eucken [62] as a function of the dynamic viscosity and the isentropic specific heat that depends on $c_{p,K}$ according to Eq. (1)

$$\kappa = \mu \cdot c_v \cdot \left(1.32 + 1.77 \cdot \frac{\mathbb{R}}{c_v}\right) \tag{11}$$

Thermal conductivity and specific heat of the solid phases are expressed as temperature dependent polynomial functions in the from $\psi = \sum_{j=0}^{n} = a_j \cdot T^j$. The polynomials have been fitted to material data provided by manufacturers [63,64] and ASPEN APV88:PURE32 Database, Table 2 provides the respective coefficients a_j.

Thermal coupling of fluid and solid regions at the interface follows two conditions that are presented in Eq. (12). First, the interface temperature is the same for both regions. Second, the continuity of heat flux over the interface is ensured by considering thermal conductivity and temperature gradient in both regions. Positive q_{rad} denotes the net radiative heat flux from the solid surface that calculates as the sum of emitted radiation and reflected fraction of the incident radiation, which is calculated according to

Eq. (16). Indices f and s denote the fluid and the solid phase, respectively. Equation (12) also applies for the coupling of two solid phases, in which case the radiative heat flux cancels out. Normal vector $\hat{n}$ is defined to point out of the fluid phase into the solid phase.

$$T_f = T_s \quad \text{and} \quad k_f \frac{dT_f}{d\hat{n}} = k_s \frac{dT_s}{d\hat{n}} + \dot{q}_{rad} \tag{12}$$

Radiative heat transfer through participating media is described by Eq. (13) [65] with radiation intensity $I(\hat{s})$ depending on direction vector $\hat{s}$.

$$\frac{dI}{ds} = \hat{s} \cdot \nabla I(\hat{s}) = \epsilon_g I_b - \beta_g I(\hat{s}) - \sigma_s I(\hat{s}) + \frac{\sigma_s}{4\pi} \int_{4\pi} I(\hat{s}') \Phi(\hat{s}', \hat{s}) d\Omega_i \tag{13}$$

Further, ϵ_g denotes the emissivity, β_g the extinction coefficient, σ_s the scattering albedo σ_s of the participating medium, and Φ the phase function [65]. In the present work, premixed, soot-free combustion of methane is considered at ambient pressure. Within the short distances between solid surfaces inside the porous structure, gas-radiation interaction is marginal. Therefore, scattering, absorption and emission by the gas phase are neglected; the heat transport equation reduces to $\hat{s} \cdot \nabla I = 0$. As a consequence, radiation intensity distribution and transferred heat are solely dependent on the boundary conditions of the gas phase.

In the present study, solid surfaces are considered as opaque, gray diffusive emitting and reflecting surfaces; the radiation intensity I_w that is directed from the solid into the fluid volume calculates as sum of surface emission, and reflection of incident radiation [65, Eq. (16.2)].

$$I_w = \epsilon_w I_{b,w} + \frac{1 - \epsilon_w}{\pi} \int_{\hat{n} \cdot \hat{s}' > 0} I(\hat{s}') \hat{n} \cdot \hat{s}' d\Omega' \tag{14}$$

with ϵ_w denoting the wall emissivity, $I_{b,w}$ the wall's integral black body irradiated intensity based on the Stefan-Boltzmann-law $I_{b,w} \cdot \pi = \sigma_{SB} \cdot T_w^4$ [65, Eq. (1.32)] with the Stefan-Boltzmann constant σ_{SB} and wall temperature T_w. The integration limit $\hat{n} \cdot \hat{s}'$ denotes the dot product of the surface normal vector and the incident radiation direction. Both vectors are defined with magnitude of unity; therefore the dot product represents the cosine of the angle formed by the two vectors. Since the surface normal vector $\hat{n}$ points out of the fluid volume, integration over positive values of the dot product covers the radiation direction vectors pointing at the surface element, respectively the incident radiation directions.

For solving the radiative heat transfer, the present study employs OpenFOAM's discrete ordinate method fvDOM [66], that discretizes the full solid angle of 4π into a finite number of angular parts with the number of azimuthal angles in a quarter sphere n_Φ and number of polar angles n_Θ. The total number of directions is $n_{rays} = 4 \cdot n_\Phi \cdot n_\Theta$ and the intervals between the discrete directions are given by

$$\Delta\Phi = \frac{\pi}{2n_\Phi} \qquad \Delta\Theta = \frac{\pi}{n_\Theta} \tag{15}$$

Radiative energy that is emitted and reflected diffusively from a solid surface, is distributed over those discrete radiation directions that point from the surface element into the fluid volume; consequently, the integrating term of Eq. (14) transforms into a summation term. Equation (16) gives the local radiative heat flux at any point of the wall r_w with w_i denoting the quadrature weights associated with the respective direction vector [65].

$$q_{rad}(r_w) \simeq \epsilon(r_w)\left(\sigma_{SB} T(r_w)^4 - \sum_{\hat{n} \cdot \hat{s}_i > 0} w_i I_i(r_w) \hat{n} \cdot \hat{s}_i\right) \tag{16}$$

In the present study, we use a symmetric set of radiation directions with $2n_\Phi = n_\Theta = 6$, yielding $\Delta\Phi = \Delta\Theta = 30°$ and a total

number of 72 rays. In a preliminary study of radiative heat transfer with representative elements of the considered porous structures, this fvDOM configuration has shown satisfactory results with relative deviation of emitted and absorbed radiative heat ranging from $7.6 \cdot 10^{-7}$ (KC) to $4.6 \cdot 10^{-4}$ (RCL). Configurations with up to 144 rays did not provide significantly improved accuracy, however computational effort increases notably with more rays.

Boundary conditions are divided into the four groups inlet face, outlet face, interface and side faces. The inlet boundary affects the fluid region and the solid region of the flame trap. For both regions, inlet face temperature are set to a fixed value of $T_{in} = 300$ K. The fluid inlet mixture with fixed species mass fractions represents premixed CH_4 and air at equivalence ratio of $\phi = 0.91$, resulting in an adiabatic flame temperature of 2147 K. Inlet pressure is set as zero gradient $\partial p_{in}/\partial \vec{n} = 0$, inlet velocity is set to a fixed value that is dependent on the actual case. Internal boundary conditions at the interface of regions follow Eq. (12) for temperature and heat flux. On the fluid side of the interface, pressure and species are treated with zero gradient, velocity follows the no-slip condition $\vec{u} = 0$. At the outlet boundary of the fluid region, velocity, temperature and species are treated with zero gradient condition normal to the face; the pressure is set to a fixed value of $p_{out} = 10^5$ Pa. All internal, inlet and outlet bounding faces of the fluid region are treated as opaque, gray and diffusive emitting surfaces, following Eq. (14). Emissivity is set to unity for inlet and outlet face, to 0.9 and 0.3 for internal interfaces with the porous structure and the flame trap, respectively [67]. Temperature applied in the first term of Eq. (14) matches the face temperature of the fluid phase for inlet and internal faces; on the outlet face this radiation temperature is set to the ambient temperature of 300 K. Lateral boundaries are treated as periodic, directly coupling translational neighboring boundary faces. Spatial derivatives are calculated in second order Gaussian integration with linear interpolation schemes. Time derivative in the fluid region follows first order Euler scheme, solid regions are simulated in steady state that does not solve for time derivatives. Simulations were initialized with gas phase and flame trap region at 300 K, and the porous structure at 1600 K. Initial gas phase composition equals the inlet, velocity was set to superficial velocity of the fresh mixture. Progress of the simulation was monitored at multiple sampling points in the fluid and solid regions. The simulation was considered as converged, when solid sampling points reached constant temperature, and fluctuations of pressure, velocity and temperature in the fluid sampling points were below 10^{-3} around the mean value for at least 10 ms of simulated time which was considered as quasi-steady state. Residuals in the transient simulated gas phase were below 10^{-8} for all species, velocity components and enthalpy, and below 10^{-6} for density, respectively. The sum of local continuity errors was below 10^{-11}.

3. Results and discussion

Simulation results provide detailed fields of fluid flow, species concentration, temperature, and heat fluxes. In the following discussion we refer to a coordinate system with axial coordinate z starting from the interface of flame trap and porous structure. Positions with positive z value are termed as 'porous structure section', while the 'flame trap region' refers to negative z values. Over all structure setups, the inlet velocity was varied from 3.0 m s^{-1} to 12.3 m s^{-1} in order to simulate four different settings of specific thermal power P_A which defines as

$$P_A = \frac{\left(\dot{m} \cdot y_f\right)_{inlet} \cdot LHV}{\Delta x \cdot \Delta y} \tag{17}$$

with mass flow rate $\dot{m}$, inlet fuel mass fraction y_f, the fuel's lower heating value LHV, and the lateral domain dimensions Δx and

Δy. With tailoring the flame trap to the porous structure, cross-sectional area ratio of ducts and solid flame trap varies between the different structure setups. As a consequence, inlet gas velocity varies between the structure setups for the same specific thermal power.

Three geometrical setups with four settings of specific thermal power each result in a total of 12 simulations that have been conducted on high performance computing clusters with up to 600 processors in parallel, consuming about $2 \cdot 10^6$ CPU-hours in total.

The next section presents and discusses the results in terms of justification of laminar flow modeling, the evaluation of net radiative flux, internal fields, and interface fluxes.

3.1. Justification of laminar flow model

For justification of the laminar flow model, focus is set on the case with highest inlet velocity that is RC-L at 903 kW m^{-2}. At the inlet, uniform values of velocity, density, and dynamic viscosity are $u = 12.3$ m s^{-1}, $\rho = 1.12$ kg m^{-3} and $\eta = 1.846 \cdot 10^{-5}$ Pa s, respectively. These values result in a Reynolds number of 746 for the duct diameter of 1 mm. Over the length of the duct, increasing gas temperature causes an increased viscosity, consequently the Reynolds number decreases. In the flame trap section, the Reynolds number is well below 2300 that is commonly considered as limiting value for laminar flow in a pipe [68]. In the porous structure region, average magnitude of the gas velocity is significantly lower due to an increased cross-sectional area of the fluid phase. For a pore diameter of approximately 6 mm the volume averaged quantities $\bar{u} = 2.6$ m s^{-1}, $\bar{\rho} = 0.193$ kg m^{-3}, and $\bar{\eta} = 6.33 \cdot 10^{-5}$ Pa give an average Reynolds number of 48.

3.2. Analysis of radiation output

For each of the three setups KC, RC-D and RC-L, four different simulations have been conducted with specific thermal power P_A ranging from 365 kW m^{-2} to 903 kW m^{-2} according to Eq. (17).

Radiation efficiency η_{rad} is defined as fraction of the thermal power that is emitted as radiative heat to the ambient. For the present simulations, η_{rad} is calculated according to Eq. (18) as the ratio of area averaged radiative flux $\bar{q}_r$ at the outlet boundary and P_A.

$$\eta_{rad} = \frac{\bar{q}_r}{P_A} = \frac{\int q_r dA_{out}}{P_A \cdot \Delta x \cdot \Delta y} \tag{18}$$

Based on the simplified model of radiative heat transfer between two infinite parallel walls of fixed temperature, for an easier interpretation of results $\bar{q}_r$ is also used to derive an effective radiation temperature T_{rad}^{eff} as function of the Stefan-Boltzmann constant $\sigma_{SB} = 5.67 \cdot 10^{-8}$ W m^{-2} K^{-4}, the outlet boundary radiation temperature $T_{rad}^{out} = 300$ K, and emissivity of porous structure $\epsilon_{por} = 0.9$

$$T_{rad}^{eff} = \left(\frac{\bar{q}_r}{\sigma_{SB} \cdot \epsilon_{por}} + \left(T_{rad}^{out}\right)^4 \right)^{0.25} \tag{19}$$

Both radiation efficiency and effective radiation temperature are shown in Fig. 2 for all simulated cases as a function of specific burner power. For all structure setups, radiation efficiency decreases with increasing burner power. For the KC setup, radiation efficiency ranges from 53.3% to 32.1%, while values for the RC setups range from 49.5% to 30.7%. Decreasing radiation efficiency indicates that a reduced share of the energy released by combustion reaction is transferred into radiative heat; as a consequence, outlet gas temperature increases with increasing burner power. Despite their difference in structure orientation, both RC setups show the same radiation efficiency for each thermal power setting. In
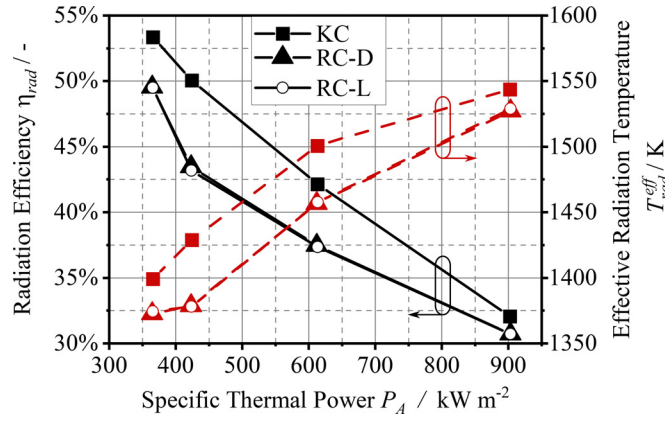
Fig. 2. Radiation Efficiency (solid lines) and Effective Radiation Temperature (dashed lines) of the simulated cases as function of specific thermal power.

contrast to the radiation efficiency, effective radiation temperature increases with increasing burner power, indicating that structure temperature and radiative flux increase with increasing burner power. Again, values for RC-D and RC-L are the same and they are lower than the respective values for the KC setup. Equal values in radiation efficiency and effective radiation temperature for both RC setups indicate that structure orientation does not show an influence on the net heat flux. Moreover, results indicate a correlation between specific surface area and radiation efficiency.

Keramiotis et al. [20] experimentally investigated a setup comprising a 10 PPI random foam structure made of Si-SiC that was operated with a $CH_4/H_2/CO/CO_2$ mixture of adiabatic flame temperatures close to CH_4 but with elevated laminar flame speed. For an equivalence ratio of 0.91 they report radiation efficiency that is 6% to 11% lower than KC related values of the present work. Yakovlev et al. [49] numerically investigated a Ni-Al alloy based radial burner porous burner. With CH_4 at equivalence ratio 1.0 they report radiation efficiency of approx. 42% at thermal load of 600 kW m^{-2} which is in good agreement with the KC structure of the present study.

3.3. Evaluation of internal fields

In order to compare the simulated cases amongst each other, three-dimensional data are transformed into one-dimensional plots along the main flow axis z. For generation of these plots, cell values of the computational domain are evaluated on 100 equidistant two-dimensional slices that are oriented perpendicular to the main flow direction. For each slice, solid and gaseous region are evaluated separately with solid temperature T_S as area weighted average value of the slice and fluid associated quantities ψ_f weighed by the absolute value of axial mass flow rate.

$$\left(\psi_f\right)_{slice} = \frac{\int_A \psi_f^* \left|\vec{u}_{fluid} \cdot \vec{n}_{slice}\right| dA_{slice}}{\int_A \left|\vec{u}_{fluid} \cdot \vec{n}_{slice}\right| dA_{slice}} \tag{20}$$

The simulation results are presented in Fig. 3 over the axial direction of the three geometry setups for varying specific thermal power. Negative values on the horizontal axis denote the flame trap related part of the domain, positive values refer to the section including the porous structure and additional space volume. The additional space separates the porous structure from the outlet boundary; thus, values related to the gas phase cover an increased range of axial coordinates.

For all cases, flame trap temperature lies above gas phase temperature (negative values on horizontal axis). Temperature level in the flame trap section decreases with increasing burner power. This trend is a result of increasing the flow rate of cold gas
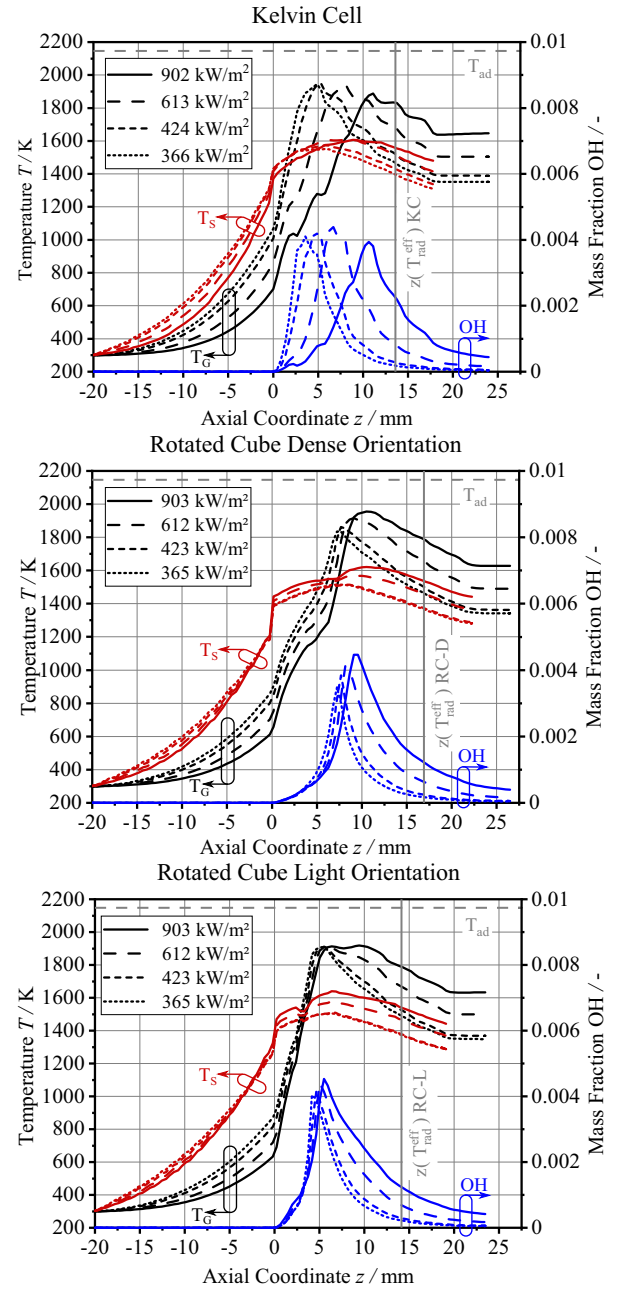

Fig. 3. Axial profiles of solid and gas temperature and OH mass fraction for the KC, RC-D and RC-L structure setup at four different values of specific burner power each.

that intensifies its cooling effect. Within the porous structure section (positive values on horizontal axis), gas temperature (black lines) exceeds solid temperature (red lines). After passing a coordinate of maximum value, both gas and solid temperature decrease towards the end of the porous structure with the solid temperature always below the gas temperature. At the end of the porous structure, both gas and solid temperature increase with increasing specific thermal power. This result is in line with Fig. 2, where an increased effective radiation temperature is found for increasing specific thermal power. Outlet gas temperature and radiation efficiency are coupled in the balance of enthalpy; with rising gas temperature, a reduced fraction of the combustion energy is available for radiative emission and radiation efficiency decreases. In all cases, OH mass fraction reaches its maximum at approximately the

same position as the gas phase temperature and solid temperature; the authors refer to this axial coordinate as the flame position. The position of the effective radiation temperature $z(T_{rad}^{eff})$ is defined as downstream axial coordinate at which $T_S = T_{rad}^{eff}$.

For the RC-L structure, flame position is 5 mm from the interface of flame trap and porous structure ($z = 0$) and almost independent of the specific thermal power. The position of effective radiation temperature is located at $z = 14.1$ mm, which is 5.4 mm from the structure end for all considered values of specific thermal power. For the RC-D structure, flame position varies in the range 7 mm to 10 mm; position of effective radiation temperature is 5.5 mm from the structure end for the range of considered specific thermal power. For the KC setup, flame position ranges from $z = 3$ mm to 11 mm; however, position of effective radiation temperature is independent from specific thermal power and located 4.4 mm from the structure end. The dependence of the flame position on the specific thermal power is a result of the geometrical details in the interaction of flame trap and porous structure. In the KC setup, no duct of the flame trap is axially aligned with a strut of the solid porous structure; the flow from the flame trap forms flow profile comparable to an expanding jet. In RC setups, the axis of the flame trap ducts point directly towards a strut of the respective structure. Consequently, the axial momentum of the affected jet is deflected into lateral momentum, which leads to an axial flame position that is independent from the flow rate. Exemplary visualizations of the flame front regions in the three-dimensional structures are included in the supplemental material Appendix A.

Porous radiant burners rely on the working principle of radiation emission from hot solid surface, but the source of heat is the combustion reaction, which takes place in the gas phase. Therefore, the gas-solid interface is evaluated on slices that are oriented normal to the main flow axis. The considered quantities ψ of interface heat flux and interface area are expressed as volume-specific values with the respective volume given by the cross-sectional area A_S of the slice and finite slice thickness Δz. With the value of Δz approaching zero, the specific quantity $\psi_{\Delta z}$ is a function of local values ψ^* and the geometric parameter l_I/A_S, as shown in the right part of Eq. (21). On a two-dimensional slice, A_S denotes the slice area and l_I the length of the interface line; thus, the parameter represents a two-dimensional analogue of the specific surface S_V. With the discretized space of a numerical simulation, it is convenient to integrate over the interface area A_I and choose discrete values of Δz for the left side of Eq. (21) in such resolution that the averaging does not obscure details of interest.

$$\psi_{\Delta z} = \frac{\int_{A_I} \psi^* dA_I}{A_S \Delta z} = \frac{1}{\Delta z} \int_z^{z+\Delta z} \int_{l_I/A_S} \psi^* d(l_I/A_S) dz$$

$$\text{with} \quad \lim_{\Delta z \to 0} \psi_{\Delta z} = \int_{l_I/A_S} \psi^* d(l_I/A_S) \tag{21}$$

In the present work, the value of Δz is systematically derived for each geometrical setup as 1% of the solid-associated extent of the domain, resulting in values of 0.38 mm, 0.42 mm, and 0.39 mm for the setups KC, RC-D and RC-L, respectively. The left side of Eq. (21) was applied to determine axial profiles of interface Temperature T_I, net radiant heat flux q_r based on absorption and emission on the solid surface, conductive heat flux q_c based on heat conductivity and temperature gradient on the gas phase side of the interface, and total heat flux q_t as sum of q_r and q_c. Axial profile of the specific surface area S_V was determined by application of Eq. (21) with ψ^* set to unity.

Figure 4 presents interface-related quantities for the three geometry setups at thermal load of 612 (613) kWm^{-2}. The horizontal axis denotes the axial coordinate with negative z-values referring the flame trap section and positive z-values referring to the section of the porous structure; a side projection of the respective
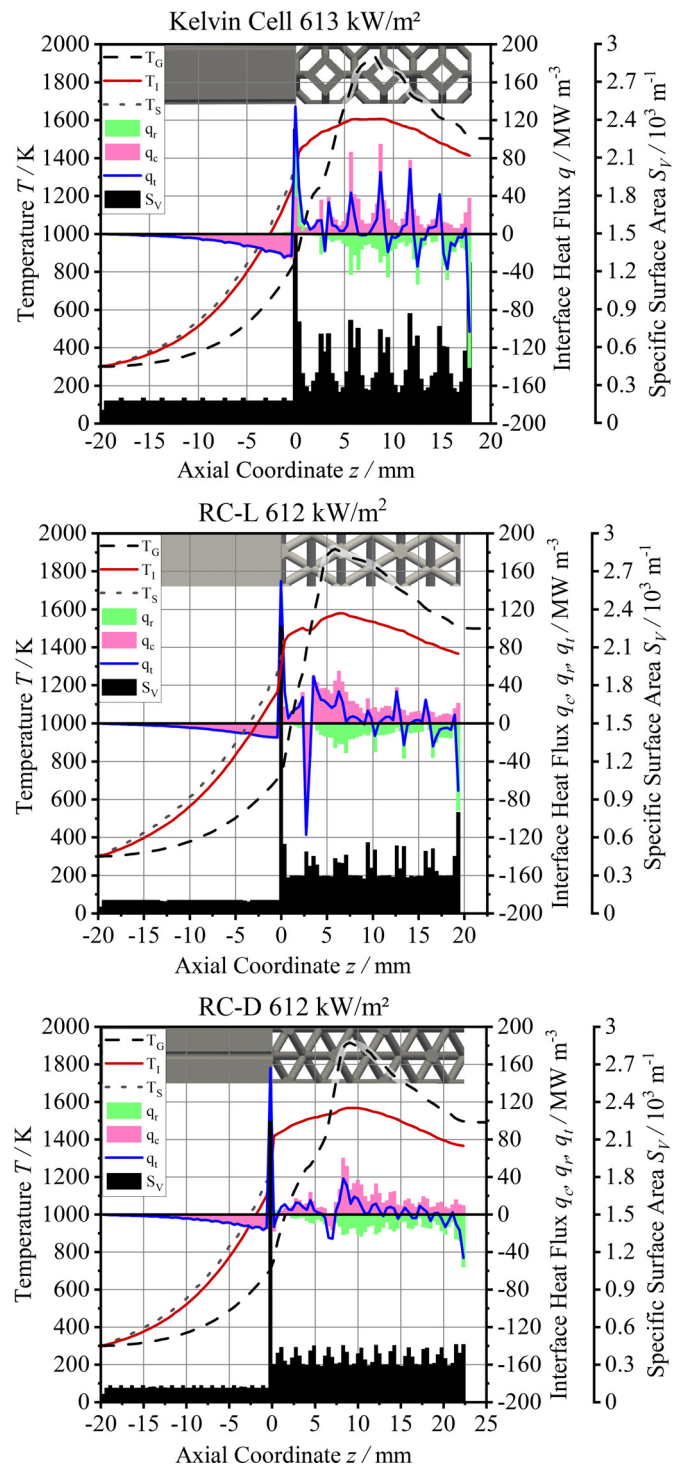

Fig. 4. Axial profiles of interface heat fluxes q_r, q_c, q_t, solid surface temperature, mass flow averaged gas phase temperature and specific surface area for the KC structure at 613 kWm^{-2}, RC-L and RC-D at specific burner power of 612 kWm^{-2}.

solid structure is provided in the background at top of each graph. A solid line denotes the interface temperature T_I that refers to the vertical axis on the left side of the graphs. The mass flow rate averaged gas phase temperature is shown for reference as dashed line. The specific surface area is shown on the bottom of the graph and refers to the second vertical axis on the right side. This quantity is presented as columns to underline averaging over the small axial interval of Δz. This also applies for the columns of radiative and

conductive heat fluxes q_r and q_c that refer to the first vertical axis on the right side. This axis provides positive values to the upper and negative values to the lower half of the graph. The total heat flux is shown as a solid line for the sake of easier distinction.

For all cases, values of the conductive heat flux q_c are negative in the flame trap section, which means that heat is transferred from the hot solid to the cold gas flow. Total heat flux q_t shows the same trend as q_c, indicating that radiative heat transfer does not contribute significantly to heat transfer inside the narrow channels of the flame trap. In the section of the porous structure, q_r is negative which shows that the structure is net emitting at any axial coordinate z except for the contact zone of flame trap and porous structure. Conductive heat transfer is positive in the section of the porous structure, indicating that heat is transferred from the gas towards the porous structure; exception of this is visible for RC-L at $z = 3$ mm and RC-D at $z = 7$ mm. These are the coordinates where cold gas jets from the flame trap hit the hot porous structure.

Specific surface area S_V shows a characteristic pattern that depends on the porous structure. RC-D is only composed of struts that are inclined towards the lateral plane, which is normal to the main flow axis. Values for S_V in the RC-D setup are varying periodically with pits at z-coordinates of strut junctions and peaks in between. In the RC-L setup, struts are oriented in the lateral plane in intervals of 3.5 mm, which are recognizable as peaks in the S_V values. The KC setup shows pronounced peaks in intervals of 3 mm; the peaks are associated with struts forming a square that is oriented in the lateral plane. At positions of increased S_V values, peaks in conductive and radiative heat flux area also present. Peaks in q_c are shifted towards the upstream edge of the S_V peak while peaks in q_r are shifted downstream. This finding matches with the mechanisms of heat transfer that scale with the available area. The flow of hot gases hits the strut on the upstream side, causing an increased transfer of heat on the concerned surface. Radiative heat transfer is determined by the temperature distribution on the surfaces that are in radiative exchange. Compared to the upstream side, the downstream side of a strut is facing more solid surface elements with lower temperature than its local value; consequently, this side of the strut net emits more radiative heat. In the porous structure section, surface temperature matches with the solid temperature in the respective case of Fig. 3; however, in the flame trap section, surface temperature is below the corresponding temperature of the solid phase. This difference indicates the presence of lateral temperature gradient in the flame trap that is due to low heat conductivity and low specific surface area.

The analysis of the gas solid interface demonstrates the impact of available surface area on both, heat transfer from gas to solid and emission of radiative heat. In the downstream section of the porous structure, surface (and solid) temperature T_S is well below the mean gas temperature T_G and conductive heat transfer q_c apparently scales with the temperature difference $T_G - T_S$ and the value of S_V. In the upstream part of the porous structure section, q_c is positive despite the fact that T_S is above T_G, implying that heat transfer takes place against the direction of the temperature gradient. This misleading part of the graph is caused by the averaging of gas temperature that is dominated by the cold jets near the flame trap. Close to the flame trap, the major part of the porous structure surface is in contact with recirculating gas that has considerably higher temperature than the mass flow averaged value at this axial position. This phenomenon is a challenge to recover by volume-averaged models that have been developed for unstructured porous media in which recirculation of hot combustion products is expected to be less pronounced due to geometrical inhibition of pronounced fresh gas jets by the random nature of the topology.

4. Conclusion

Detailed three-dimensional numerical simulations of two layer radiant porous burners have been performed in order to investigate the impact of structure parameters on heat transfer and radiative output. Resolved consideration of both the flame trap and the porous body granted detailed insight on pore scale level into conditions and processes inside the porous burner. A skeletal chemical reaction mechanism was employed for adequate heat release representation of premixed combustion of methane at equivalence ratio $\phi = 0.91$. Spatially resolved radiative heat transfer between solid surface was accounted for by the fvDOM model, employing gray radiation on 72 discrete ordinates. Three regular structure setups were considered as periodic representative elements in lateral directions and with full extension of flame trap and porous structure in axial direction. With progress in additive manufacturing, the application of structured porous media is expected to gain growing attention also in porous burner applications. This work provides detailed data sets for three structured setups. The present study focuses on the impact of the porous structure on the radiative output in a two layer porous burner.

- It is shown that the radiative output of the burner (expressed as effective radiation temperature T_{rad}^{eff}) increases with increasing thermal load. However, with increasing thermal load, the radiation efficiency decreases which results in elevated flue gas temperature. Determined radiation efficiency of the Kelvin Cell structure is in line with comparable literature data for a thin layered radial porous burner.
- Results imply that radiation efficiency depends on the structure's specific surface area (Kelvin Cell vs. Rotated Cube structure), but not on the orientation of the structure that is formed by a network of cylindrical struts (Rotated Cube in dense vs light setup).
- Simulation results show the maximum solid temperature from 1510 K to 1640 K which is far below the adiabatic flame temperature of 2147 K for the considered cases. Optimization of the structure temperature towards the maximum operating temperature of the solid material (1723 K for Si-SiC [69]) bears potential to improve radiative output and radiative efficiency.
- Radiation output can be translated into an effective radiation temperature that is found on the axial profile of solid temperature in a certain axial distance from the downstream end of the structure. This distance depends on the structure geometry but is independent from specific thermal power or flame position in the considered cases.
- Interface heat fluxes are shown in high axial resolution and are quantified with respect to the individual contribution of the different heat transfer mechanisms. Both convective and radiative heat transfer are phenomena related to the available interphase area; simulation results recover the beneficial impact of increased surface area on the individual mechanisms of heat transfer and suggest that heat transfer from gas to solid can be improved through appropriate design of the flow field. Thorough discussion of such designs will be subject to future work.
- Volume-averaged presentation of interface heat fluxes reveals challenge of structured porous media for volume-averaged models to recover appropriate heat transfer near the interface of the two solid layers.

Declaration of Competing Interest

The authors declare that they have no known competing financial interests or personal relationships that could have appeared to influence the work reported in this paper.

Acknowledgment

Supplementary material

Supplementary material associated with this article can be found, in the online version, at 10.1016/j.combustflame.2022.112370.

References

[1] G.W. Phelps, J.B. Wachtman, Ceramics, general survey, in: Wiley-VCH (Ed.), Ullmann's Encyclopedia of Industrial Chemistry, John Wiley & Sons, Ltd, Weinheim (2000), pp. 593–637.

[2] G. Gochev, V. Ulaganathan, R. Miller, Foams, in: Wiley-VCH (Ed.), Ullmann's Encyclopedia of Industrial Chemistry, John Wiley & Sons, Ltd, Weinheim (2000), pp. 1–31.

[3] E. Werzner, M.A. Mendes, S. Ray, D. Trimis, Numerical investigation on the depth filtration of liquid metals: influence of process conditions and inclusion properties, Adv. Eng. Mater. 15 (2013) 1307–1314.

[4] A. Sommers, Q. Wang, X. Han, C. T'Joen, Y. Park, A. Jacobi, Ceramics and ceramic matrix composites for heat exchangers in advanced thermal systems–a review, Appl. Therm. Eng. 30 (2010) 1277–1291.

[5] Z.G. Wu, C.Y. Zhao, Experimental investigations of porous materials in high temperature thermal energy storage systems, Sol. Energy 85 (2011) 1371–1380.

[6] D. Liu, Q. Li, Y. Xuan, Reticulated porous volumetric solar receiver designs guided by normal absorptance and hemispherical volumetric emittance investigations, Int. J. Heat Mass Transf. 114 (2017) 1067–1071.

[7] Y. Huang, C.Y.H. Chao, P. Cheng, Effects of preheating and operation conditions on combustion in a porous medium, Int. J. Heat Mass Transf. 45 (2002) 4315–4324.

[8] J. Binner, Ceramic foams, in: M. Scheffler, P. Colombo (Eds.), Cellular Ceramics: Structure, Manufacturing, Properties and Applications, WILEY-VCH (2005), pp. 33–56.

[9] A. Ortona, C. D'Angelo, S. Gianella, D. Gaia, Cellular ceramics produced by rapid prototyping and replication, Mater. Lett. 80 (2012) 95–98.

[10] A.L. Avila-Marin, J. Fernandez-Reche, S. Gianella, L. Ferrari, D. Sanchez-Señoran, Experimental study of innovative periodic cellular structures as air volumetric absorbers, Renew. Energy 184 (2022) 391–404.

[11] A. Kesting, K. Pickenäcker, D. Trimis, I. Cerri, R. Krieger, H. Schneider, Development of a highly efficient gas infrared heater by means of combustion in inert porous media, Int. Gas Res. Conf. Proc. (2001).

[12] A. Fuessel, H. Klemm, D. Boettge, F. Marschallek, J. Adler, A. Michaelis, Advancement of cellular ceramics made of silicon carbide for burner applications, IOP Conf. Ser. - Mat. Sci. 18 (2011) 182001.

[13] D. Trimis, O. Pickenäcker, K. Wawrzinek, Porous burners, in: M. Scheffler, P. Colombo (Eds.), Cellular Ceramics: Structure, Manufacturing, Properties and Applications, WILEY-VCH (2005), pp. 484–507.

[14] Z. Al-Hamamre, S. Diezinger, P. Talukdar, F.V. Issendorff, D. Trimis, Combustion of low calorific gases from landfills and waste pyrolysis using porous medium burner technology, Process Saf. Environ. 84 (2006) 297–308.

[15] S. Voß, Z. Al-Hamamre, D. Trimis, Charakterisierung des Emissionsverhaltens und der Verbrennungsstabilität von Schwach- und Mittelgasen in Porenbrennern, Gaswärme Int. 56 (2007) 200–204.

[16] N. Djordjevic, P. Habisreuther, N. Zarzalis, Porous burner for application in stationary gas turbines: an experimental investigation of the flame stability, emissions and temperature boundary condition, Flow Turbul. Combust. 89 (2012) 261–274.

[17] C. Bedoya, I. Dinkov, P. Habisreuther, N. Zarzalis, H. Bockhorn, P. Parthasarathy, Experimental study, 1D volume-averaged calculations and 3D direct pore level simulations of the flame stabilization in porous inert media at elevated pressure, Combust. Flame 162 (10) (2015) 3740–3754.

[18] V. Khanna, R. Goel, J.L. Ellzey, Measurements of emissions and radiation for methane combustion within a porous medium burner, Combust. Sci. Technol. 99 (1994) 133–142.

[19] C. Keramiotis, B. Stelzner, D. Trimis, M. Founti, Porous burners for low emission combustion: an experimental investigation, Energy 45 (2012) 213–219.

[20] C. Keramiotis, M. Katoufa, G. Vourliotakis, A. Hatziapostolou, M.A. Founti, Experimental investigation of a radiant porous burner performance with simulated natural gas, biogas and synthesis gas fuel blends, Fuel 158 (2015) 835–842.

[21] A. Maznoy, A. Kirdyashkin, S. Minaev, A. Markov, N. Pichugin, E. Yakovlev, A study on the effects of porous structure on the environmental and radiative characteristics of cylindrical Ni-Al burners, Energy 160 (2018) 399–409.

[22] A. Loukou, I. Frenzel, J. Klein, D. Trimis, Experimental study of hydrogen production and soot particulate matter emissions from methane rich-combustion in inert porous media, Int. J. Hydrogen Energy 37 (2012) 16686–16696.

[23] S. Voss, M.A. Mendes, J.M. Pereira, S. Ray, J.C. Pereira, D. Trimis, Investigation on the thermal flame thickness for lean premixed combustion of low calorific H2/CO mixtures within porous inert media, Proc. Combust. Inst. 34 (2013) 3335–3342.

[24] F. Sirotkin, R. Fursenko, S. Kumar, S. Minaev, Flame anchoring regime of filtrational gas combustion: theory and experiment, Proc. Combust. Inst. 36 (2017) 4383–4389.

[25] J. Kiefer, M.C. Weikl, T. Seeger, F.V. Issendorff, F. Beyrau, A. Leipertz, Non-intrusive gas-phase temperature measurements inside a porous burner using dual-pump cars, Proc. Combust. Inst. 32 (2009) 3123–3129.

[26] B. Stelzner, C. Keramiotis, S. Voss, M.A. Founti, D. Trimis, Analysis of the flame structure for lean methane–air combustion in porous inert media by resolving the hydroxyl radical, Proc. Combust. Inst. 35 (2015) 3381–3388.

[27] J. Dunnmon, S. Sobhani, M. Wu, R. Fahrig, M. Ihme, An investigation of internal flame structure in porous media combustion via X-ray computed tomography, Proc. Combust. Inst. 36 (2017) 4399–4408.

[28] R.V. Fursenko, I.A. Yakovlev, E.S. Odintsov, S.D. Zambalov, S.S. Minaev, Pore-scale flame dynamics in a one-layer porous burner, Combust. Flame 235 (2022).

[29] M.R. Henneke, J.L. Ellzey, Modeling of filtration combustion in a packed bed, Combust. Flame 117 (1999) 832–840.

[30] A.J. Barra, G. Diepvens, J.L. Ellzey, M.R. Henneke, Numerical study of the effects of material properties on flame stabilization in a porous burner, Combust. Flame 134 (2003) 369–379.

[31] A.J. Barra, J.L. Ellzey, Heat recirculation and heat transfer in porous burners, Combust. Flame 137 (2004) 230–241.

[32] X.Y. Zhou, J.C. Pereira, Numerical study of combustion and pollutants formation in inert nonhomogeneous porous media, Combust. Sci. Technol. 130 (1997) 335–364.

[33] M.A. Mendes, J.M. Pereira, J.C. Pereira, A numerical study of the stability of one-dimensional laminar premixed flames in inert porous media, Combust. Flame 153 (2008) 525–539.

[34] N. Djordjevic, P. Habisreuther, N. Zarzalis, A numerical investigation of the flame stability in porous burners employing various ceramic sponge-like structures, Chem. Eng. Sci. 66 (2011) 682–688.

[35] N. Wakao, S. Kaguei, Heat and mass transfer in packed beds, Gordon and Breach Science Publications, New York, 1982.

[36] K. Kamiuto, S.S. Yee, Heat transfer correlations for open-cellular porous materials, Int. Commun. Heat Mass 32 (2005) 947–953.

[37] J. Grosse, B. Dietrich, G.I. Garrido, P. Habisreuther, N. Zarzalis, H. Martin, M. Kind, K.C. Bettina, Morphological characterization of ceramic sponges for applications in chemical engineering, Ind. Eng. Chem. Res. 48 (2009) 10395–10401.

[38] P. Parthasarathy, P. Habisreuther, N. Zarzalis, Identification of radiative properties of reticulated ceramic porous inert media using ray tracing technique, J. Quant. Spectrosc. Radiative Transf. 113 (2012) 1961–1969.

[39] P. Parthasarathy, P. Habisreuther, N. Zarzalis, Evaluation of longitudinal dispersion coefficient in open-cell foams using transient direct pore level simulation, Chem. Eng. Sci. 90 (2013) 242–249.

[40] M.F. Fidalgo, M.A. Mendes, J.M. Pereira, An automated method for efficient multi-parametric analysis of porous radiant burner performance, Int. J. Therm. Sci. 163 (2021) 106851.

[41] I. Malico, X.Y. Zhou, J.C. Pereira, Two-dimensional numerical study of combustion and pollutants formation in porous burners, Combust. Sci. Technol. 152 (2000) 57–79.

[42] J. Ferguson, S. Sobhani, M. Ihme, Pore-resolved simulations of porous media combustion with conjugate heat transfer, Proc. Combust. Inst. 38 (2021) 2127–2134.

[43] Y. Liu, Y. Deng, J. Shi, R. Xiao, H. Li, Pore-level numerical simulation of methane-air combustion in a simplified two-layer porous burner, Chinese J. Chem. Eng. 34 (2021) 87–96.

[44] M. Sahraoui, M. Kaviany, Direct simulation vs volume-averaged treatment of adiabatic, premixed flame in a porous medium, Int. J. Heat Mass Transf. 37 (IX) (1994) 2817–2834.

[45] Q. Li, J. Wang, J. Li, J. Shi, Fundamental numerical analysis of a porous micro–combustor filled with alumina spheres: pore-scale vs. volume-averaged models, Appl. Sci. 11 (16) (2021).

[46] E. Miyata, N. Fukushima, Y. Naka, M. Shimura, M. Tanahashi, T. Miyauchi, Direct numerical simulation of micro combustion in a narrow circular channel with a detailed kinetic mechanism, Proc. Combust. Inst. 35 (3) (2015) 3421–3427.

[47] S.N. Hoda, S.A. Gandjalikhan Nassab, J.J. Ebrahim, Three dimensional numerical simulation of combustion and heat transfer in porous radiant burners, Int. J. Therm. Sci. 145 (2019).

[48] I. Yakovlev, S. Zambalov, Three-dimensional pore-scale numerical simulation of methane-air combustion in inert porous media under the conditions of upstream and downstream combustion wave propagation through the media, Combust. Flame 209 (2019) 74–98.

[49] I. Yakovlev, A. Maznoy, S. Zambalov, Pore-scale study of complex flame stabilization phenomena in thin-layered radial porous burner, Combust. Flame 231 (2021) 111468.

[50] P.L. Billerot, L. Dufresne, R. Lemaire, P. Seers, 3D CFD analysis of a diamond lattice-based porous burner, Energy 207 (2020).

[51] A. Banerjee, D. Paul, Developments and applications of porous medium combustion: a recent review, Energy 221 (2021) 119868.

[52] A. Ortona, D. Trimis, V. Uhlig, R. Eder, S. Gianella, P. Fino, G. D'Amico, E. Boulet, C. Chazelas, T. Grämer, E. Cresci, J.G. Wüunning, H. Altena, F. Beneke, M. Debier, SiSiC heat exchangers for recuperative gas burners with highly structured surface elements, Int. J. Appl. Ceram. Tec. 11 (2014) 927–937.

[53] T. Fischedick, M. Kind, B. Dietrich, Radial two-phase thermal conductivity of ceramic sponges up to high temperatures experimental results and correlation, Int. J. Therm. Sci. 114 (2017) 98–113.

[54] M. Scheffler, P. Colombo, Cellular ceramics: structure, manufacturing, properties and applications, WILEY-VCH, Weinheim, 2005.

[55] M. Pelanconi, E. Rezaei, A. Ortona, Cellular ceramic architectures produced by hybrid additive manufacturing: a review on the evolution of their design, J. Ceram. Soc. Jpn. 128 (2020) 595–604.

[56] H.G. Weller, G. Tabor, H. Jasak, C. Fureby, A tensorial approach to computational continuum mechanics using object-oriented techniques, Comput. Phys. 12 (1998) 620.

[57] P. Stephan, K. Schaber, K. Stephan, F. Mayinger, Thermodynamik Grundlagen und technische Anwendungen Band 1: Einstoffsysteme, Springer-Verlag, Berlin, 2009.

[58] J. Warnatz, U. Maas, R. Dibble, Combustion, 4th ed., Springer-Verlag, Berlin, 2006.

[59] R.W. Bilger, S.H. Stårner, R.J. Kee, On reduced mechanisms for methane-air combustion in non-premixed flames, Combust. Flame 80 (1990) 135–149.

[60] B. McBride, S. Gordon, M. Reno, Coefficients for calculating thermodynamic and transport properties of individual species, Technical Report, NASA Lewis Research Center, Cleveland, OH, 1993. http://ntrs.nasa.gov/archive/nasa/casi.ntrs.nasa.gov/19940013151_1994013151.pdf

[61] F.M. White, Fluid mechanics, WCB McGraw-Hill, Boston, 1999.

[62] B.E. Poling, J.M. Prausnitz, J.P. O'Connell, The properties of gases and liquids, McGraw-Hill Education, New York, 2001.

[63] EngiCer S.A., Material data sheet: SiSiC, http://www.engicer.com/wp-content/uploads/materialdata-sheet/EngiCer_Material_Data_Sheet_SiSiC.pdf.

[64] duoTherm Stark Isoliersysteme GmbH & Co KG, duoForm HT180 (Mullit)https://duotherm-gmbh.de/downloads/datenblaetter/duobase-datenblaetter.html.

[65] M.F. Modest, Radiative heat transfer, Academic Press, Amsterdam, 2003.

[66] G.D. Raithby, E.H. Chui, A finite-volume method for predicting a radiant heat transfer in enclosures with participating media, J. Heat Transf. 112 (1990) 415–423.

[67] K. Pickenäcker, Emissionsarme kompakte Gasheizsysteme auf der Basis stabilisierter Verbrennung in porösen Medien, Fortschritt-Berichte VDI.: Reihe 6, Energietechnik, VDI-Verlag, D"usseldorf, 2001.

[68] VDI-GVC, VDI-Wärmeatlas, Springer, Heidelberg, 2013.

[69] S. Gianella, D. Gaia, A. Ortona, High temperature applications of Si-SiC cellular ceramics, Adv. Eng. Mater. 14 (2012) 1074–1081.